PCCP

ROYAL SOCIETY OF CHEMISTRY

PAPER

View Article Online
View Journal | View Issue

Check for updates

Cite this: *Phys. Chem. Chem. Phys.*, 2023, **25**, 22744

The impact of non-adiabatic effects on reaction dynamics: a study based on the adiabatic and non-adiabatic potential energy surfaces of CaH_2^+

Di He, *[a] Wentao Li, [b] Quanjiang Li,[a] Shenghui Chen,[a] Li Wang, [a] Yanli Liu [a] and Meishan Wang*[a]

Received 26th May 2023,
Accepted 9th August 2023

DOI: 10.1039/d3cp02416d

rsc.li/pccp

The two-state non-adiabatic potential energy matrices of the CaH_2^+ system are calculated *via* a diabatization approach by using a neural network model. Subsequently, the adiabatic and non-adiabatic potential energy surfaces (PESs) are constructed based on these non-adiabatic potential energy matrices. Furthermore, based on the adiabatic and non-adiabatic PESs, the $Ca^+(4s^2S) + H_2(X^1\Sigma_g^+) \rightarrow H(^2S) + CaH^+(X^1\Sigma^+)$ reaction is studied using the time-dependent wave packet method. Comparative analysis of the experimental and theoretical integral reaction cross-sections (ICSs) indicates that the maximum deviation between the results obtained from the adiabatic PES and the corresponding experimental value is 12.7 bohr^2; in contrast, the maximum discrepancy between the theoretical result derived from the non-adiabatic PES and the experimental value is merely 0.42 bohr^2. The potential well along the reaction path acts as a 'filter', selectively guiding intermediates with longer lifetimes in the potential well back to the reactant channel. This phenomenon indicates that the non-adiabatic effects significantly influence the reaction dynamics of the CaH_2^+ system.

1. Introduction

With the increasing prominence and growing depth of research on elementary reactions, the investigation of reaction dynamics has progressively become diverse. Over the past few decades, chemical reactions occurring on adiabatic potential energy surfaces (PESs) have become the research hotspot. With the advancement in non-adiabatic theory and enhancement of computational capabilities, researchers are now capable of constructing non-adiabatic PESs with remarkable accuracy. Consequently, research on non-adiabatic dynamics has also experienced significant advancement in recent decades.[1–14] In most elementary reaction dynamics calculations, it is imperative to consider non-adiabatic effects for obtaining meaningful results. However, some theoretical calculations of reaction dynamics by using solely adiabatic PESs can still produce sound theoretical outcomes that align well with the experimental results.[15,16] This suggests that the influence of non-adiabatic effects on reaction dynamics varies across different systems. For comprehensive analysis of the impact of non-adiabatic effects on chemical reactions where both reactants and products exist on the same adiabatic PES, it is essential to investigate the reaction dynamics of the same chemical reaction on both adiabatic and non-adiabatic PESs. Notably, the characteristics of PESs differ among various reactions; therefore, the extent to which non-adiabatic effects influence different reactions also differs.

Due to the very long-range asymptotic region between hydrogen-like ions and H_2 molecules, the reaction between an alkaline-earth metal atom and a H_2 molecule constitutes an ideal candidate for researching atom–diatom collisions under cold and ultra-cold conditions.[17–29] Non-adiabatic transitions often occur in an elementary reaction process; therefore, if non-adiabatic effects are not considered in theoretical calculations, the obtained theoretical results may significantly differ from the experimental results. For instance, in experiments, the integral cross-section (ICS) of the Li + HCl → LiH + Cl reaction is 27 Å^2 at a collision energy of 2.7 kcal mol^{-1}.[30] However, the theoretical results obtained using two different adiabatic PESs correspond to approximately 4 Å^2, which is much smaller than the experimental one.[31,32] The ICS of the $Ca^+ + H_2 \rightarrow CaH^+ + H$ reaction obtained in the experiment is about 0.15 Å^2 at a collision energy of 4.5 eV.[25] Recently, an ICS of the $Ca^+ + H_2 \rightarrow CaH^+ + H$ reaction calculated from a quantum dynamics work based on an adiabatic PES is 3.3 Å^2, which is 22 times larger than the experimental result.[33] The main objective of this study is to investigate whether the significant difference in the ICS between the adiabatic PES calculation and the experimental

---

[a] School of Physics and Optoelectronics Engineering, Ludong University, Yantai 264025, China. E-mail: mswang1971@163.com, hedi@ldu.edu.cn

[b] Weifang University of Science and Technology, Shouguang 262700, China

result can be attributed to the presence of non-adiabatic effects. For this purpose, both the adiabatic and non-adiabatic PESs of the CaH_2^+ system are constructed. The state-to-state dynamics of the $Ca^+(4s^2S) + H_2(X^1\Sigma_g^+) \rightarrow H(^2S) + CaH^+(X^1\Sigma^+)$ reaction is calculated based on the non-adiabatic PES. At the same time, for comparing the non-adiabatic effects, the quantum dynamics of the same reaction on the adiabatic PES are also calculated. For the convenience of discussion, the reactions involved in this article are designated as follows:

$$Ca^+(4s^2S) + H_2(X^1\Sigma_g^+) \rightarrow H(^2S) + CaH^+(X^1\Sigma^+), \quad \text{(R1a)}$$

$$Ca^+(4s^2S) + H_2(X^1\Sigma_g^+) \rightarrow H(^2S) + CaH^+(X^1\Sigma^+), \quad \text{(R1b)}$$

$$Ca^+(4s^2S) + H_2(X^1\Sigma_g^+) \rightarrow Ca^+(4s^2S) + H_2(X^1\Sigma_g^+), \quad \text{(R2)}$$

$$Ca^+(4s^2S) + H_2(X^1\Sigma_g^+) \rightarrow Ca^+(3d^2D) + H_2(X^1\Sigma_g^+), \quad \text{(R3)}$$

where the (R1a) reaction takes place on the adiabatic PES and (R1b), (R2), and (R3) reactions take place on the non-adiabatic PES.

This paper is organized as follows: Section II provides the construction details of the PES and the diabatization scheme, and introduces the characteristics of the PES in detail. Section III presents the dynamics results in detail and provides an in-depth analysis of the dynamics results. Section IV presents the conclusions.

2. Potential energy surfaces

2.1 *Ab initio* calculations

In *ab initio* calculations, in order to consider the relativistic effects of the inner electrons in Ca^+ ions, the aug-cc-pwCVTZ basis set is selected for Ca^+ ions, while the aug-cc-pVTZ basis set is utilized for H atoms. In the *ab initio* calculations, the multi-reference configuration interaction method is used to treat the dynamic correlation,[34] while the state-averaged complete active space self-consistent field (SA-CASSCF) method is used to treat the static correlation.[35] In the SA-CASSCF calculations, five electronic states ($1^2A'$, $2^2A'$, $1^4A'$, $1^2A''$, and $2^2A''$) with equal weight and three valence electrons are considered. A total of 17 orbitals are included in the CASSCF calculations; 9 (7a′ + 2a″) of them are double-occupied and the remaining 8 (5a′ + 3a″) are active orbitals. In order to compensate for the impact of higher-order correlation, the final *ab initio* energy is included with Davidson correction.

Finally, 19265 points are calculated to construct the PES. All *ab initio* calculations in this study are carried out by using the MOLPRO package.[36]

2.2 Diabatization scheme & PES fitting

Many non-adiabatic theories have been developed so far. The main objective of these theories is to find the adiabatic–diabatic transformation matrix. The energy under the adiabatic representation can be converted to the non-adiabatic representation through the transformation matrix. Considering the case of a two-state system as an example, the specific transformation formula is as follows:

$$\begin{pmatrix} V_{11} & V_{12} \\ V_{21} & V_{22} \end{pmatrix} = T \begin{pmatrix} E_1 & 0 \\ 0 & E_2 \end{pmatrix} T^{\mathrm{H}}, \quad (1)$$

where T denotes the adiabtic–diabatic transformation matrix:

$$T = \begin{pmatrix} \cos\alpha & -\sin\alpha \\ \sin\alpha & \cos\alpha \end{pmatrix}, \quad (2)$$

where α is the mixing angle. Obviously, the mixing angle is the key point of the diabatization scheme. Many different methods are available to calculate the mixing angle; some methods are based on non-adiabatic coupling matrix elements, some methods are based on adiabatic eigenfunction coefficients, and the remaining methods are based on molecular properties.[37]

In this study, the neural network (NN) method is adopted to construct non-adiabatic PESs. To the best of our knowledge, it is the one which has been widely used in the construction of adiabatic PESs. However, the NN method has been rarely applied to the construction of non-adiabatic PESs. This may be attributed to the fact that it is a very complex process to obtain the potential matrix elements. This study provides a brief introduction about the application of the NN method in the construction of non-adiabatic PESs, and a more detailed introduction can be found in the relevant literature reports.[38–41] The artificial NN generally consists of three parts, namely the input layer, the hidden layer and the output layer. To consider the exchange symmetry of identical atoms, the fundamental invariants (FIs) method is used in the calculations. The FIs are generated by using the following functions:

$$x_1^0 = r_{\mathrm{CaH}_a} + r_{\mathrm{CaH}_b}, \quad (3)$$

$$x_2^0 = {r_{\mathrm{CaH}_a}}^2 + {r_{\mathrm{CaH}_b}}^2, \quad (4)$$

$$x_3^0 = r_{\mathrm{HH}}, \quad (5)$$

where x_i^0 = (i = 1–3) is the input signals of the input layer. The hidden layer contains a large number of neurons with adjustable parameters (weight and bias), which is initially randomly generated. In this study, there are two hidden layers in the NN model and 30 neurons are included in each hidden layer. The NN functions can be expressed as follows:

$$y_i^m = \sum_{j=1}^{S^{m-1}} \left(w_{i,j}^m a_j^{m-1}\right) + b_i^m, a_i^m = f^m\left(x_i^m\right), \quad (6)$$

where $w_{i,j}^m$ is the connection weight between the jth neuron of the $(m-1)$th layer and the ith neuron of the mth layer, b_i^m is the bias of the ith neuron of the mth layer, and y_i^m and a_i^m are the input and output of the ith neuron of the mth layer, respectively. The transfer function $f(x)$ is a hyperbolic tangent function.

$$f(x) = \frac{e^x - e^{-x}}{e^x + e^{-x}} \quad (7)$$

In the construction of an adiabatic PES, there is only one output term (E_{fit}), while in the construction of two-states non-adiabatic PESs, there are three output terms, namely potential matrix elements V_{11}, V_{22} and V_{12}. Then, the fitted energies are obtained by using the following formulas:

$$E_{\text{fit}}^{1} = \frac{V_{11}^{\text{d}} + V_{22}^{\text{d}}}{2} + \frac{1}{2}\sqrt{\left(V_{22}^{\text{d}} - V_{11}^{\text{d}}\right)^{2} + 4V_{12}^{\text{d}2}}, \tag{8}$$

$$E_{\text{fit}}^{2} = \frac{V_{11}^{\text{d}} + V_{22}^{\text{d}}}{2} - \frac{1}{2}\sqrt{\left(V_{22}^{\text{d}} - V_{11}^{\text{d}}\right)^{2} + 4V_{12}^{\text{d}2}}. \tag{9}$$

The NN parameters are optimized by minimizing the following performance index

$$P = \sum_{q=1}^{Q}\sum_{I=1}^{N^{\text{state}}}\left[E_{I}^{(\text{fit})} - E_{I}^{(\text{ab})}\right]^{2} \tag{10}$$

where Q is the number of geometries and $E_{I}^{(\text{ab})}$ denotes the *ab initio* energies.

For the two-state case, it is considered that $V_{12}^{\text{d}} = V_{21}^{\text{d}}$. In addition, there is an additional constraint for the coupling term V_{12}^{d}, that is, the line integral of the derivative coupling along a closed loop around a conical intersection should yield a value of π:[41]

$$\oint_{C}\tau(R)\cdot \text{d}R = \pi, \tag{11}$$

When the integral path tends to be infinitely small, the integral path C becomes a very small circle. At this time, eqn (11) can be changed into the following form:

$$\oint_{0}^{2\pi}\tau(\varphi|\rho)\text{d}\varphi = \pi, \tag{12}$$

where ρ is the radius of the small circle and φ denotes the polar angle. The derivative coupling can be expressed as follows:[41]

$$\tau(\varphi|\rho) = \frac{1}{2}\cdot\left[1 + \left(\frac{2V_{12}^{\text{d}}}{V_{11}^{\text{d}} - V_{22}^{\text{d}}}\right)^{2}\right]^{-1}\cdot \times\frac{2\left[\frac{\partial V_{12}^{\text{d}}}{\partial\varphi}\left(V_{11}^{\text{d}} - V_{22}^{\text{d}}\right) - V_{12}^{d}\left(\frac{\partial V_{11}^{\text{d}}}{\partial\varphi} - \frac{\partial V_{22}^{\text{d}}}{\partial\varphi}\right)\right]}{\left(V_{11}^{\text{d}} - V_{22}^{\text{d}}\right)^{2}} \tag{13}$$

To guarantee the appropriate behavior of the coupling term V_{12}^{d} near the $C_{2\text{v}}$ configurations, a multiplicative factor, cos(θ), is adopted in this study, which can also guarantee that the off-diagonal terms are anti-symmetry for θ in [0, 2π]. The refined functional form for these three terms is written as follows:

$$V_{11}^{\text{d}} = \text{NN}_{1}(\text{FI}) \tag{14}$$

$$V_{22}^{\text{d}} = \text{NN}_{2}(\text{FI}) \tag{15}$$

$$V_{12}^{\text{d}} = \text{NN}_{3}(\text{FI})\cos\theta \tag{16}$$

where $\text{NN}_{i}(\text{FI})$ are NN functions of FIs, and θ is the Jacobi angle.

2.3 Topological characteristics of the potential energy surface

The three-dimensional contour maps of the V_{11} and V_{22} surfaces are presented in Fig. 1 at Ca–H–H angles of 60°, 90°, 120°, and 180°, respectively. The zero-point of the potential energy is set at the dissociation limit of the three atoms. The valleys at the left and right ends of the V_{11} surface correspond to $\text{Ca}^{+}(4\text{s}^{2}\text{S}) + \text{H}_{2}(\text{X}^{1}\Sigma_{\text{g}}^{+})$ and $\text{H}~(^{2}\text{S}) + \text{CaH}~(\text{A}^{1}\Sigma^{+})$, respectively. The valleys at the left and right ends of the V_{22} surface correspond to $\text{Ca}^{+}(3\text{d}^{2}\text{D}) + \text{H}_{2}(\text{X}^{1}\Sigma_{\text{g}}^{+})$ and $\text{H}(^{2}\text{S}) + \text{CaH}^{+}(\text{X}^{1}\Sigma^{+})$, respectively. It is evident from the figure that the studied reaction initiates at the left end of the V_{11} surface, undergoes a transition in the interaction region to the V_{22} surface, and finally yields the product at the right end of the V_{22} surface. Additionally, it can be observed that the seam of the two PESs shifts with the change in the Ca–H–H angle. In order to analyze the reaction process more precisely, the minimum energy paths (MEPs) corresponding to the PESs shown in Fig. 1 are illustrated in Fig. 2.

In Fig. 2, the black curves represent the MEPs on the V_{11} surface, and the red curves represent the MEPs on the V_{22} surface. The potential energy difference between the reactant $\text{Ca}^{+}~(4\text{s}^{2}\text{S}) + \text{H}_{2}~(\text{X}^{1}\Sigma_{\text{g}}^{+})$ channel and the product $\text{H}(^{2}\text{S}) + \text{CaH}(\text{X}^{1}\Sigma^{+})$ channel is about 2.5 eV, which decreases to about 2.32 eV when considering the zero-point energy of the ground state H_{2} molecule and the ground state $\text{CaH}^{+}(\text{X}^{1}\Sigma^{+})$ molecule. After further examination of the four subplots in Fig. 2, it is evident that the position of the crossover point between the two MEPs is subject to change with variations in the Ca–H–H angle. At an angle of 60°, the crossover point is situated at the bottom of the potential well on the V_{22} surface. However, as the Ca–H–H angle increases, the potential well on the V_{22} surface progressively becomes shallower, and the crossover point gradually shifts toward the top of the potential barrier on the V_{22} surface.

The aforementioned diagrams illustrate that the reaction studied herein takes place on the ground state adiabatic PES $1^{2}\text{A}'$ of the $\text{CaH}_{2}{}^{+}$ system. Fig. 3a shows the adiabatic PES for the motion of a Ca^{+} ion around a H_{2} molecule when the bond length of the HH molecule is 7.32 bohr. Fig. 3b shows the adiabatic PES for the motion of the H ion around a CaH^{+} molecule when the bond length of the CaH^{+} molecule is 5.06 bohr. The coordinate origins of Fig. 3a and b are set at the center of the H_{2} molecule and the center of the CaH molecule, respectively. The minimum potential energy shown in Fig. 3a is located in the middle region of the hydrogen molecule, indicating that the Ca^{+} ion tends to approach the H_{2} molecule along a direction perpendicular to the HH bond. Fig. 3b exhibits the presence of potential wells around both the Ca^{+} ion and the H atom. However, it is evident that the potential well around the hydrogen atom is deeper than that around the Ca^{+} ion, and the farther away it is from the Ca^{+} ion, the lower the potential energy.

3. Reaction dynamics

3.1 Dynamical calculations

The time-dependent wave packet (TDWP) method employed in this study was developed by Zhang *et al.* and improved by

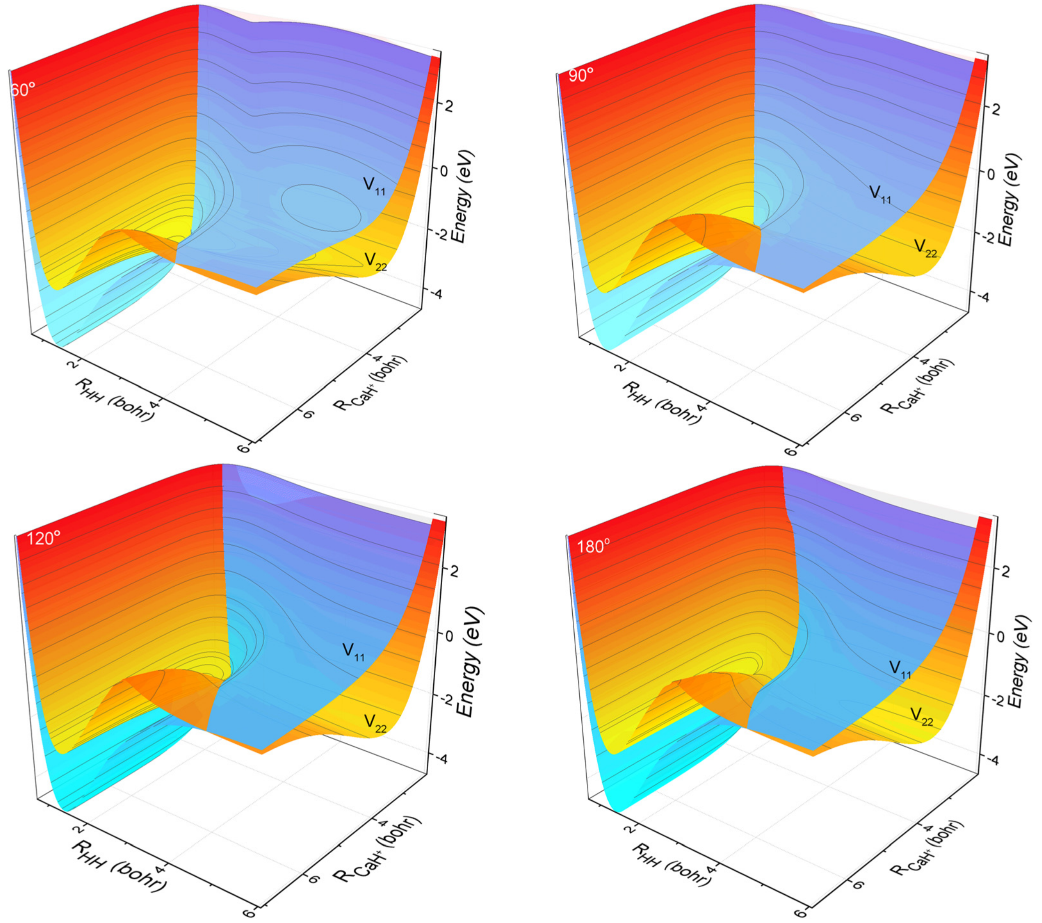

Fig. 1 3D PESs of the non-adiabatic states V_d^{11} and V_d^{22} for Ca–H–H with bond angles of 60.0°, 90.0°, 120.0° and 180.0°.

Sun *et al.*[42,43] The TDWP method has been proven to be a reliable and efficient method for theoretical calculations of elementary reaction dynamics. Herein, the main focus is on the dynamics, while a detailed introduction of the TDWP method can be found in previous relevant literature reports.[42,43] In the TDWP method, the body-fixed Jacobi coordinate is employed to represent the wave functions. The coordinates for the reactant A + BC are represented by $\boldsymbol{R}$, $\boldsymbol{r}$, and $\boldsymbol{\theta}$, where $\boldsymbol{R}$ is the length from A to the BC center of mass, $\boldsymbol{r}$ is the BC bond length, and $\boldsymbol{\theta}$ represents the angle between $\boldsymbol{R}$ and $\boldsymbol{r}$. In this study, the propagation of the wave packets is performed in the coordinates of the reactant. A dividing surface is set in the product region, and detailed dynamics information can be obtained by calculating the scattering wave functions that reach the dividing surface. To prevent the wave packets reaching the grid boundary along $\boldsymbol{R}$ and $\boldsymbol{r}$, the absorption potentials are placed at the end of each channel. The dynamics calculations of the title reaction are performed based on adiabatic and diabatic PESs, respectively. In addition, a number of convergence tests have been carried out on both adiabatic and non-adiabatic PESs. Table 1 lists the converged parameters obtained from the TDWP calculations based on the adiabatic PES, while Table 2 summarizes the converged parameters based on the non-adiabatic PES. In Tables 1 and 2, the N_R^{tot}, N_r^{tot} and j represent the total grid points in $\boldsymbol{R}$, $\boldsymbol{r}$, and $\boldsymbol{\theta}$ degrees of freedom, respectively. N_R^{int} and N_r^{int} represent the grid points in the interaction region along the $\boldsymbol{R}$ and $\boldsymbol{r}$ direction, respectively. R_0 and Δ_R denote the position and width of the initial wave packet, respectively. E_0 represents the energy at the center of the wave packet. The absorbing potential is an exponential function which can be expressed as follows:

$$D(r)=\begin{cases}\exp\left[-\Delta_t\cdot C_a\cdot\left(\dfrac{r-r_a}{r_b-r_a}\right)^n\right], & r_a\le r\le r_b\\ \exp\left[-\Delta_t\cdot C_b\cdot\left(\dfrac{r-r_b}{r_{\text{end}}-r_b}\right)^n\right]+\exp[-\Delta_t\cdot C_a], & r_b\le r\le r_{\text{end}}.\end{cases}\tag{17}$$

In the present calculations, the maximum total angular momentum is 99, which is large enough to ensure convergence of the calculations in the range with a collision energy of less than 4.5 eV.

3.2 Dynamics results

The reaction probabilities for the (R1a) and (R1b) reactions are depicted in Fig. 4a and b, respectively. The observed reaction probability threshold aligns with the previous MEPs result, and the probability gradually increases as the collision energy rises.

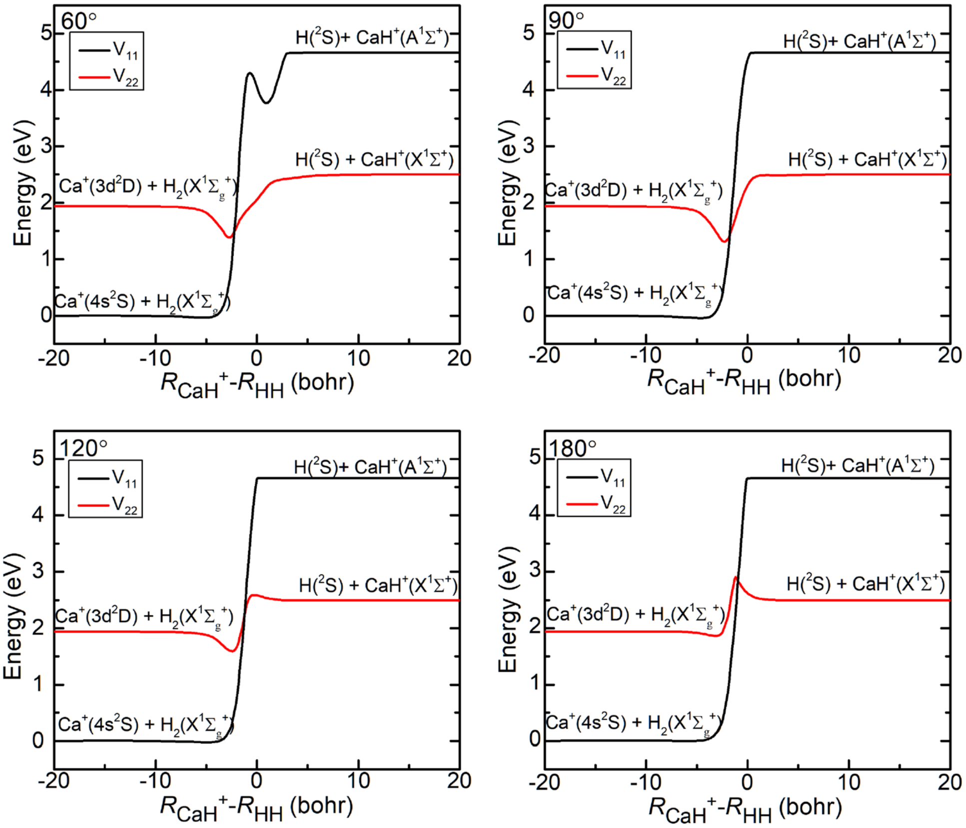

Fig. 2 Minimum energy paths of V_d^{11} and V_d^{22} for the Ca–H–H angle fixed at 60.0°, 90.0°, 120.0° and 180.0°.

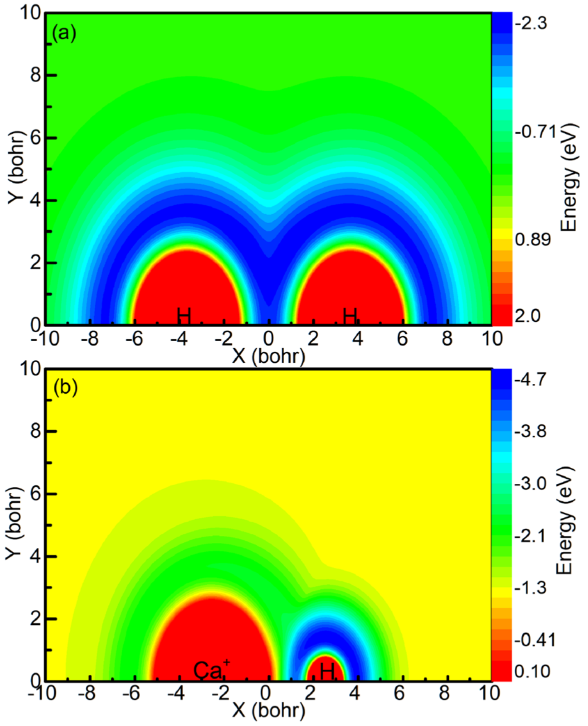

Fig. 3 (a) Contour plot for a Ca^+ ion moving around a HH molecule fixed at R_{HH} = 7.32 bohr and lying along the *x*-axis. (b) Color plot for a H atom moving around a CaH^+ molecule ion fixed at R_{CaH} = 5.06 bohr. The dissociation limit of the CaH_2^+ molecule ion is set as the zero point of potential energy.

Table 1 Numerical parameters used in the adiabatic dynamics calculations

Grid/basis range and size	$R \in [0.01\text{ a.u.}, 18.0\text{ a.u.}]$, $N_R^{tot} = 255$, $N_R^{int} = 199$
	$r \in [0.01\text{ a.u.}, 18.0\text{ a.u.}]$, $N_r^{tot} = 255$, $N_r^{int} = 79$
	$j_{min} = 0 \sim j_{max} = 120$
Initial wavepacket	$R_0 = 12.0$ a.u, $\varDelta_R = 0.\ 2$ a.u., $E_0 = 3.6$ eV
Absorbing potential in *R* coordinate	$n = 2$ $C_a^R = 0.12$ $C_b^R = 0.07$ $R_a = 14.0$ $R_b = 17.0$
Absorbing potential in *r* coordinate	$n = 2$ $C_a^r = 0.1$ $C_b^r = 0.2$ $r_a = 14.0$ $r_b = 17.0$
Total propagation time	22 000 a.u.
Time step	$\varDelta_t = 10$ a.u.

Table 2 Numerical parameters used in the non-adiabatic dynamics calculations

Grid/basis range and size	$R \in [0.01\text{ a.u.}, 18.0\text{ a.u.}]$, $N_R^{tot} = 255$, $N_R^{int} = 145$
	$r \in [0.01\text{ a.u.}, 18.0\text{ a.u.}]$, $N_r^{tot} = 179$, $N_r^{int} = 79$
	$j_{min} = 0 \sim j_{max} = 120$
Initial wavepacket	$R_0 = 12.0$ a.u, $\varDelta_R = 0.\ 22$ a.u., $E_0 = 3.5$ eV
Absorption functions in *R* coordinate	$n = 2$ $C_a^R = 0.1$ $C_b^R = 0.07$ $R_a = 14.0$ $R_b = 17.0$
Absorption functions in *r* coordinate	$n = 2$ $C_a^R = 0.1$ $C_b^R = 0.2$ $R_a = 14.9$ $R_b = 17.9$
Total propagation time	10 000 a.u.
Time step	10 a.u.

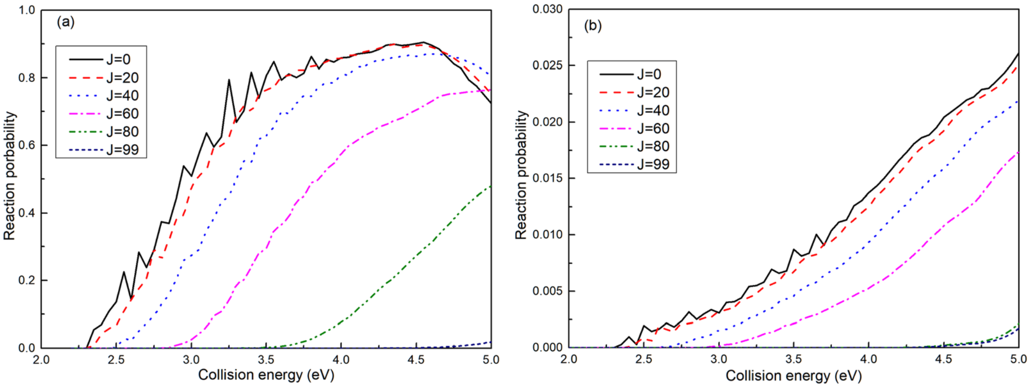

Fig. 4 Reaction probabilities of the $Ca^+(4s^2S) + H_2(X^1\Sigma_g^+) \rightarrow H(^2S) + CaH^+(X^1\Sigma^+)$ reaction calculated from adiabatic PES (a) and non-adiabatic PES (b).

Upon comparing the reaction probabilities at different total angular momenta, it becomes evident that both (R1a) and (R1b) reactions exhibit higher thresholds with increasing total angular momentum. This trend is attributed to the growing centrifugal potential as the total angular momentum increases, which leads to the increase in the minimum energy required to initiate the chemical reaction. Additionally, it is notable that the reaction probabilities of the (R1a) reaction are significantly greater than those of the (R1b) reaction.

To assess the distribution of the wave packet among different channels on the non-adiabatic PES, Fig. 5 illustrates the reaction probabilities for (R1b), (R2), and (R3) reactions at a total angular momentum of $J = 0$. From Fig. 5, it is evident that the probability of the wave packet returning to the reactant channel (R2) significantly outweighs the probabilities of those entering the excited state channel of the Ca^+ ion (R3) and the product channels ((R1b)). Furthermore, the probability of the wave packet entering the product channel slightly surpasses that of entering the excited state channel of the Ca^+ ion. Based on the MEPs shown in Fig. 2 and the reaction probabilities presented in Fig. 5, herein, a plausible reaction mechanism is proposed; *i.e.*, the wave packet enters the interaction region through the reactant channel, and undergoes non-adiabatic transitions at the intersection of the two PESs, and then transitions from the ground state to the first excited state. However, since the intersection is just in the potential well of the excited PES, the wave packet transitioning to the first excited state is trapped in the potential well. Owing to the confinement of the potential well, most wave packets oscillate within the potential well and eventually return to the reactant channel, with only a small fraction entering the product channel. The potential well in the excited state functions as a 'filter', selectively guiding wave packets with longer lifetimes in the potential well back to the ground state PES, thereby yielding a significantly higher probability of returning to the reactant channel.

The ICSs for the (R1a) and (R1b) reactions are illustrated in Fig. 6, alongside the experimental results reported by Georgiadis *et al.*[25] Apparently, the ICS of the (R1b) reaction exhibits a significantly better agreement with the experimental data compared to the ICS of the (R1a) reaction. This indicates that the results obtained based on non-adiabatic PES are more in line with

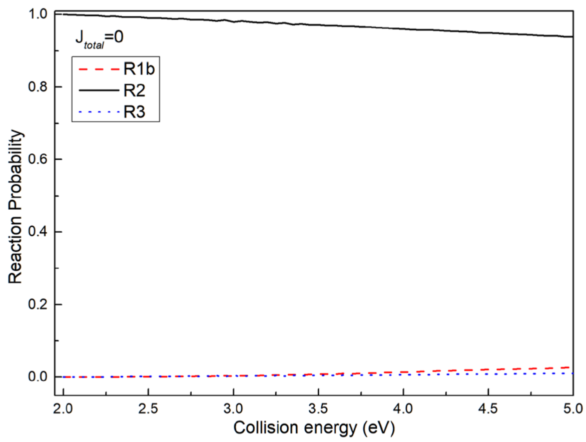

Fig. 5 Reaction probabilities of (R1b), (R2) and (R3) reactions at total angular momentum $J = 0$.

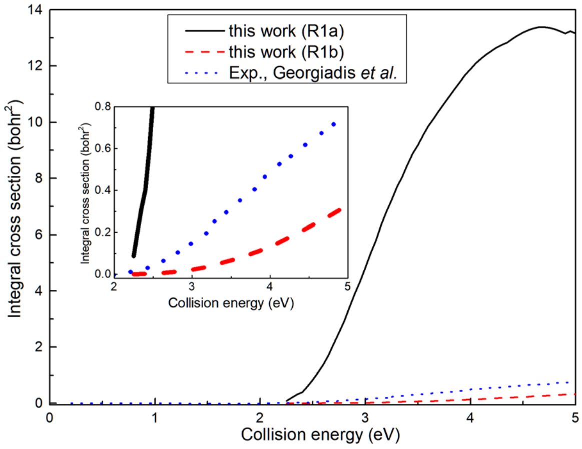

Fig. 6 Total ICSs of the $Ca^+(4s^2S) + H_2(X^1\Sigma_g^+) \rightarrow H(^2S) + CaH^+(X^1\Sigma^+)$ reaction calculated from the adiabatic PES and non-adiabatic PES compared with experimental values.

the actual situation. However, it can also be observed that the deviation between the ICS of the (R1b) reaction and the experimental value increases gradually with the increase of the collision energy. In our calculations, the H_2 molecule is in its rovibrational ground state, while in the experiment, the rotational energy of the H_2 molecule is about 0.024 eV, which may account for the difference between the ICS of the (R1b) reaction and the experimental results. Within the collision energy range below 4.6 eV, the ICS of the (R1a) reaction increases rapidly as a function of collision energy. However, when the collision energy exceeds 4.6 eV, the ICS of the (R1a) reaction gradually diminishes with a further increase in collision energy. This phenomenon can be attributed to the increasing proportion of wave packets entering the dissociation channel as the collision energy exceeds 4.6 eV, resulting in a decline in ICS. Simultaneously, the ICS of the (R1b) reaction continues to increase with the collision energy, even after exceeding 4.6 eV. When the collision energy is greater than the dissociation energy of the product molecule, the reaction can still yield the $H(^2S)$ + $CaH^+(X^1\Sigma^+)$ product, indicating that a portion of the collision energy has been converted into the relative translational energy between the

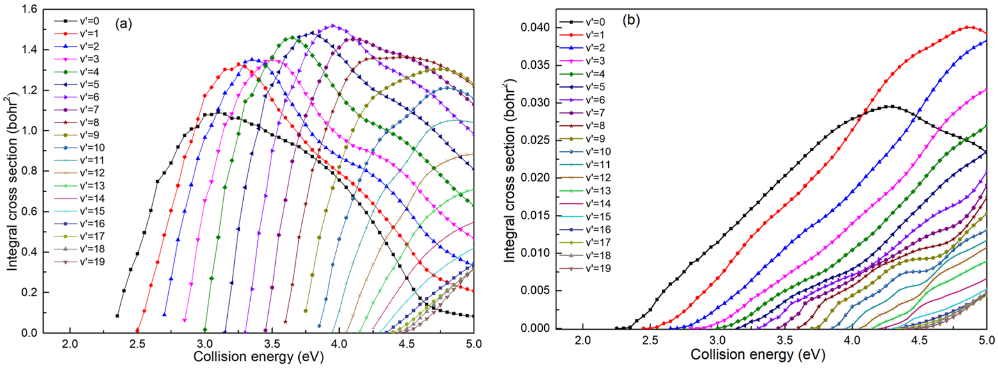

Fig. 7 Vibrational state-resolved ICSs of the $Ca^+(4s^2S)$ + $H_2(X^1\Sigma_g^+)$ → $H(^2S)$ + $CaH^+(X^1\Sigma^+)$ reaction calculated based on the adiabatic PES (a) and non-adiabatic PES (b).

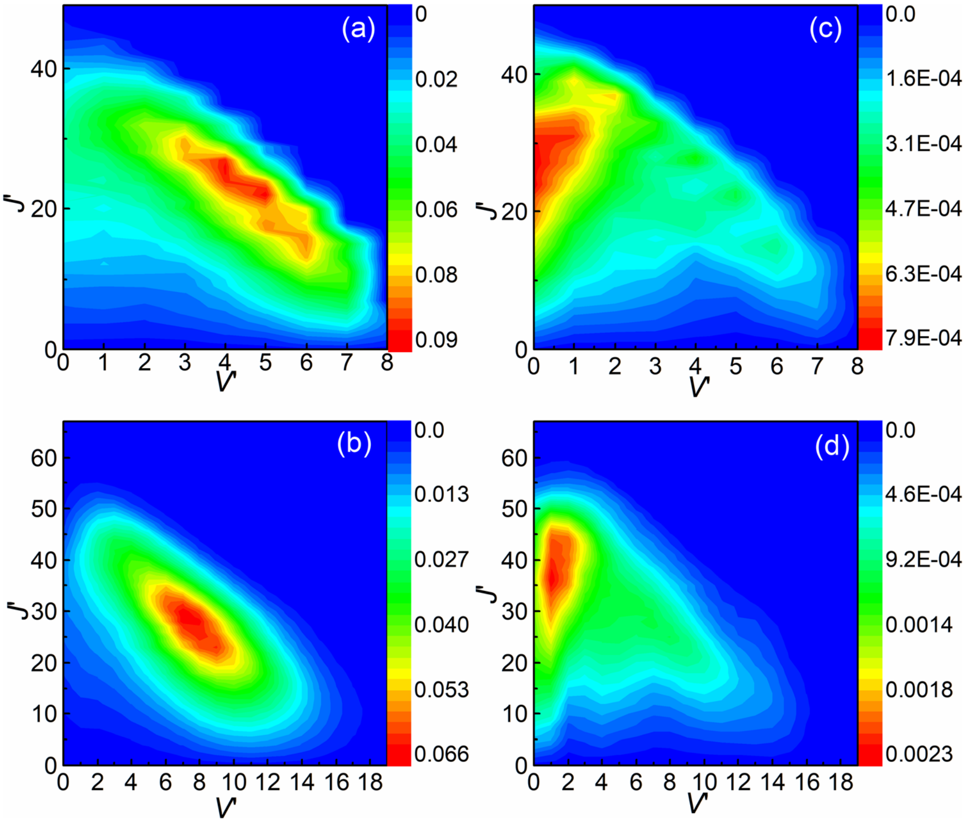

Fig. 8 Rovibrational state resolved ICSs of the (R1a) (left panels) and (R1b) (right panels) reaction at the collision energies of 3.6 and 4.5 eV.

H atom and CaH^+ molecule, while the remaining energy is converted into the internal energy of the CaH^+ molecule, which is below its dissociation energy.

Based on the analysis of Fig. 6, it is evident that the conversion of collision energy into internal energy of the product molecules is more efficient in the (R1a) reaction compared to that in the (R1b) reaction. In order to gain a better understanding of these distinct reaction mechanisms based on the two types of PESs, vibrational state-resolved ICSs are further computed. The vibrational state-resolved ICS obtained from the adiabatic and non-adiabatic PESs are depicted in Fig. 7a and b, respectively. From Fig. 7a, it is observed that the vibrational state with the highest population increases as the collision energy increases. In contrast, Fig. 7b reveals that within the collision energy range below 4.0 eV, the vibrational state with the highest population remains $\nu' = 0$. However, as the collision energy continues to increase, it shifts to $\nu' = 1$. The result presented in Fig. 7b indicates that collision energy cannot be effectively converted into the vibrational energy of the CaH^+ molecule on non-adiabatic PES. Based solely on the results shown in Fig. 7, it is not clear how energy is distributed during the process, and more detailed information on the product molecules is needed.

The rovibrational state-resolved ICSs are presented in Fig. 8. The results calculated at collision energies of 3.6 and 4.5 eV are shown in the upper and lower panels, respectively. The left and right panels depict the results of (R1a) and (R1b) reactions, respectively. The rovibrational state-resolved ICSs of the (R1a) reaction exhibit a peak corresponding to a lower rotational quantum number compared to the (R1b) reaction at the same collision energy. These results indicate that in the non-adiabatic reaction, the collision energy is predominantly converted into the rotational energy of the CaH^+ molecules during the conversion from the intermediate to the product. By combining the findings from Fig. 7 and 8, it can be inferred that the (R1b) reaction yields product molecules with higher relative translational energy compared to the (R1a) reaction.

The analysis of the reaction mechanism relies on the indispensable information provided by the differential cross-section (DCS). Fig. 9 exhibits the DCSs at collision energies of 3.6 and 4.5 eV. Similar to the previous figure, the left panels (Fig. 9a and b) display the results for the (R1a) reaction, while the right panels (Fig. 9c and d) depict the results for the (R1b) reaction. The CaH^+ molecules generated on the adiabatic PES exhibit a pronounced forward scattering trend, whereas the value for backward and sideways scattering can be almost ignored. The CaH^+ molecules generated on the non-adiabatic PES also exhibit significant forward scattering, but the sideways and backward scattering distributions are different from the previous case and cannot be ignored. By comparing the reaction

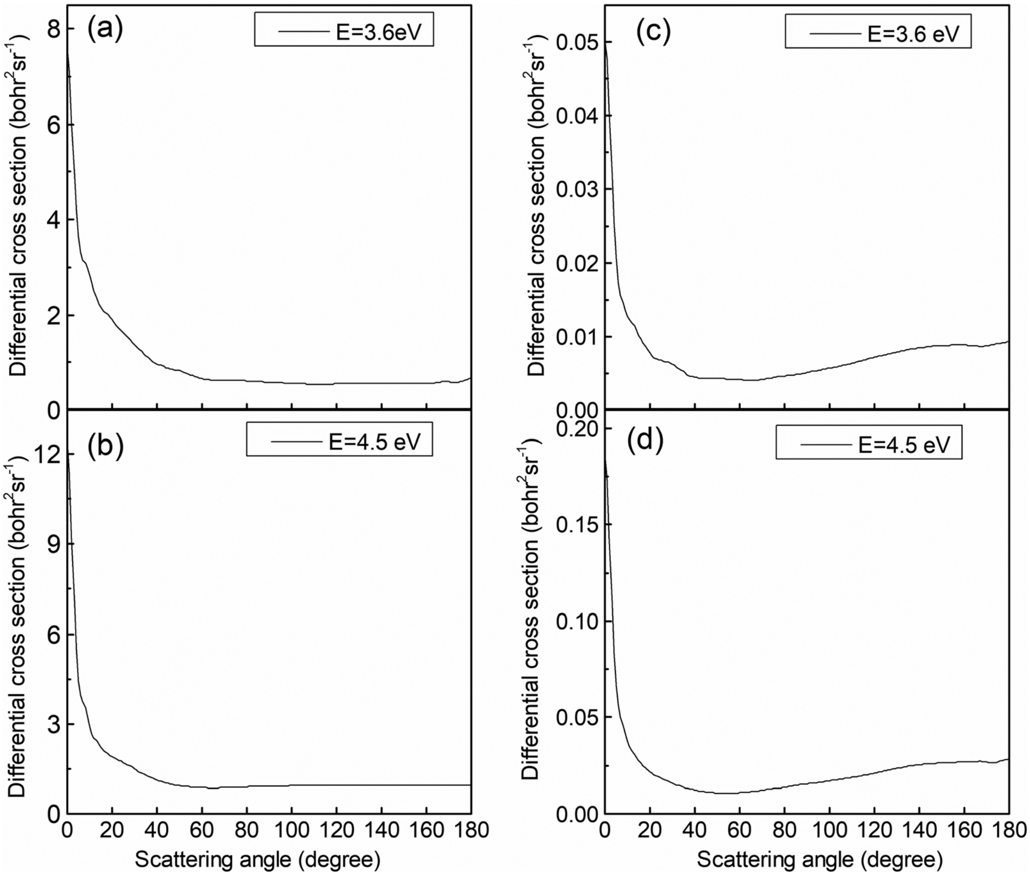

Fig. 9 DCSs of the (R1a) (left panels) and (R1b) (right panels) reaction at the collision energies of 3.6 and 4.5 eV.

paths of the (R1a) and (R1b) reactions, it becomes apparent that the (R1a) reaction lacks a potential well along its reaction path. Furthermore, due to the substantial difference in mass between the Ca^+ ion and the H_2 molecule, the velocity direction of the CaH^+ molecule is primarily determined by the velocity of the Ca^+ ion, resulting in evident forward scattering in the (R1a) reaction. Generally, the longer the life of intermediate products in the potential well, the more likely the scattering direction of product molecules exhibits significant isotropy. However, there is a potential well on the reaction path of the (R1b) reaction, which is just in the intersection area of two non-adiabatic PESs. This potential well acts as a 'filter' for the intermediate products, guiding long-lived intermediates back into the reactant molecular channel while short-lived intermediates swiftly escape the potential well and transform into products. The DCS on the non-adiabatic PES for the (R1b) reaction exhibits a prominent forward scattering peak, along with noticeable values for backward and forward scattering, indicating the presence of two distinct reaction mechanisms within the (R1b) reaction.

To verify our hypothesis, the vibrational state-resolved DCS for a collision energy of 4.5 eV is presented in Fig. 10. Fig. 10a and b depict the results calculated from (R1a) and (R1b) reactions, respectively. In Fig. 10a, it is evident that the peak of forward scattering is centered around $\nu' = 8$. Fig. 10b reveals a striking similarity in the forward scattering distribution to that observed in Fig. 10a. Additionally, Fig. 10b demonstrates that for both backward and sideways scattering, the CaH^+ molecules primarily concentrate around the vibrational level $\nu' = 2$. Moreover, the distribution of backward and sideways scattering is broader compared to that of forward scattering. Consequently, this accounts for the vibrational state-resolved ICS peak being at $\nu' = 2$ instead of $\nu' = 8$ at a collision energy of 4.5 eV for the (R1b) reaction, as depicted in Fig. 8.

The forward scattering distribution in the (R1a) reaction closely resembles that of the forward scattering in the (R1b) reaction, suggesting consistency in the reaction mechanisms of the (R1a) reaction and the reaction responsible for generating forward scattering molecules in the (R1b) reaction. The main difference in the vibrational energy level distribution arises from the sideways and backward scattering of CaH^+ molecules. In the (R1b) reaction, the CaH^+ molecules that scatter backward and sideways possess lower vibrational energy levels. This observation indirectly implies that the majority of the collision energy is converted into relative translational energy between the H atom and CaH^+ molecule. One possible reaction process is that the intermediate product composed of H atoms and CaH^+ molecules contains a large rotational energy before escaping the potential well. With the separation of the H atom and CaH^+ molecule, this rotational energy is transformed into relative translational energy between the H atom and CaH^+ molecule. From the contour plot presented in Fig. 3b, it is evident that when the H atom rotates around the CaH^+ molecule, it tends to depart from the CaH^+ molecule along the path with smaller changes in the potential energy gradient, *i.e.*, away from the CaH^+ molecule at the end of the Ca^+ ion. Consequently, this reaction mechanism contributes to the prevalence of sideways or backward scattering in the CaH^+ molecules.

4. Conclusion

We investigate the state-to-state dynamics of the $Ca^+(4s^2S) + H_2(X^1\Sigma_g^+) \rightarrow H(^2S) + CaH^+(X^1\Sigma^+)$ reaction on both adiabatic and non-adiabatic PESs that we constructed. The calculations reveal that the reaction probability and the obtained ICS on the adiabatic PES are significantly higher compared to those on the non-adiabatic PES. These results indicate that non-adiabatic effects have a profound influence on the $Ca^+(4s^2S) + H_2(X^1\Sigma_g^+) \rightarrow H(^2S) + CaH^+(X^1\Sigma^+)$ reaction. This influence arises due to the intersection seam of the non-adiabatic PES being precisely located within the potential well of the excited-state adiabatic PES. Consequently, intermediate products with longer lifetimes within the well show a high probability of returning to the reactant channel, resulting in substantial differences in reaction probability and ICS between the

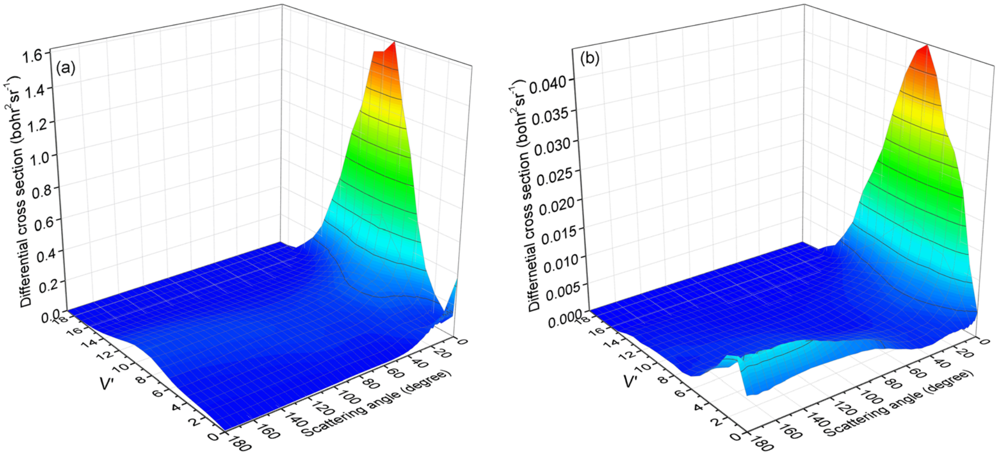

Fig. 10 Vibrational state-resolved DCSs of the (R1a) (left panel) and (R1b) (right panel) reaction at a collision energy of 4.5 eV.

reactions occurring on the adiabatic and non-adiabatic PESs. Furthermore, we have conducted calculations for the vibrational and vibrational-rotational state-resolved ICSs of the reaction on both the adiabatic and non-adiabatic PESs. The results of the vibrational state-resolved ICSs show that the collision energy can be more effectively converted into the internal energy of the molecule in the reaction on the adiabatic PES. On the other hand, the results of the vibrational-rotational state-resolved ICS reveal that the intermediates in the reaction on the non-adiabatic PES tend to distribute the collision energy to the rotational degree of freedom of the product molecule. Based on the results of the DCS and vibrational state-resolved DCS, two different reaction mechanisms are identified in the reaction on the non-adiabatic PES. One mechanism is dominated by the Ca^+ ion, which inserts into the H_2 molecule bond to form an intermediate product. In this collision mechanism, the collision energy can be effectively converted into the vibrational energy of the product molecule. However, most of these intermediate products exhibit longer lifetimes in the potential well and only a small fraction of them can smoothly transform into the product molecule. The CaH^+ molecule generated by this mechanism shows almost the same velocity direction as the incident Ca^+ ion, which leads to a significant forward scattering in the DCS. The other mechanism involves the Ca^+ ion capturing an H atom at one end of the H_2 molecule to form a CaH^+ molecule. Moreover, the other H atom does not immediately separate from the CaH^+ molecule but rotates around it and eventually separates from the Ca atom at the other end of the molecule. This mechanism effectively converts the collision energy into a relative translational energy between the H atom and the CaH^+ molecule, and the CaH^+ molecules generated by this mechanism exhibit significant sideways and backward scattering.

Conflicts of interest

There are no conflicts of interest to declare.

Acknowledgements

This work was supported by the National Natural Science Foundation of China (grant no. 12274191)

References

1 P. Halvick and D. G. Truhlar, *J. Chem. Phys.*, 1992, **96**, 2895–2909.

2 C. Maierle, G. C. Schatz, M. S. Gordon, P. McCabe and J. Connor, *J. Chem. Soc., Faraday Trans.*, 1997, **93**, 709–720.

3 S. Gray, C. Petrongolo, K. Drukker and G. Schatz, *J. Phys. Chem. A*, 1999, **103**, 9448–9459.

4 S. A. Nizkorodov, W. W. Harper, W. B. Chapman, B. W. Blackmon and D. J. Nesbitt, *J. Chem. Phys.*, 1999, **111**, 8404–8416.

5 M. Hack and D. Truhlar, *J. Phys. Chem. A*, 2000, **104**, 7917–7926.

6 S. Mahapatra, H. Köppel, L. Cederbaum, P. Stampfuss and W. Wenzel, *Chem. Phys.*, 2000, **259**, 211–226.

7 G. C. Schatz, B. Fisher, W. Grande, K. Kumayama and L. A. Pederson, *J. Phys. Chem. A*, 2001, **105**, 2515–2521.

8 C. R. Evenhuis, X. Lin, D. H. Zhang, D. Yarkony and M. A. Collins, *J. Chem. Phys.*, 2005, **123**, 134110.

9 R. F. Lu, T. S. Chu and K. L. Han, *J. Phys. Chem. A*, 2005, **109**, 6683–6688.

10 T. S. Chu, K. L. Han and G. C. Schatz, *J. Phys. Chem. A*, 2007, **111**, 8286–8290.

11 S. Y. Lin, H. Guo, B. Jiang, S. Zhou and D. Xie, *J. Phys. Chem. A*, 2010, **114**, 9655–9661.

12 Z. Sun, S. Y. Lin and Y. Zheng, *J. Chem. Phys.*, 2011, **135**, 234301.

13 P. Y. Zhang and K. L. Han, *J. Phys. Chem. A*, 2013, **117**, 8512–8518.

14 H. Guo and D. R. Yarkony, *Phys. Chem. Chem. Phys.*, 2016, **18**, 26335–26352.

15 T. Yang, J. Chen, L. Huang, T. Wang, C. Xiao, Z. Sun, D. Dai, X. Yang and D. H. Zhang, *Science*, 2015, **347**, 60–63.

16 Z. Sun and D. H. Zhang, *Int. J. Quantum Chem.*, 2015, **115**, 689–699.

17 H. S. Lee, Y. S. Lee and G. H. Jeung, *J. Phys. Chem. A*, 1999, **103**, 11080–11088.

18 T. J. Martínez, *Chem. Phys. Lett.*, 1997, **272**, 139–147.

19 M. Ben-Nun, T. Martinez and R. Levine, *J. Phys. Chem. A*, 1997, **101**, 7522–7529.

20 S. Bililign, P. Kleiber, W. Kearney and K. Sando, *J. Chem. Phys.*, 1992, **96**, 218–229.

21 L. H. Fan, J. J. Chen, Y. Y. Lin and W. T. Luh, *J. Phys. Chem. A*, 1999, **103**, 1300–1305.

22 B. Roth, P. Blythe, H. Wenz, H. Daerr and S. Schiller, *Phys. Rev. A*, 2006, **73**, 042712.

23 P. F. Staanum, K. Højbjerre, R. Wester and M. Drewsen, *Phys. Rev. Lett.*, 2008, **100**, 243003.

24 M. Satta, M. Marquéz-Mijares, E. Yurtsever, S. Bovino and F. A. Gianturco, *Int. J. Mass Spectrom.*, 2013, **351**, 47–55.

25 R. Georgiadis and P. Armentrout, *J. Phys. Chem.*, 1988, **92**, 7060–7067.

26 A. K. Hansen, M. A. Sørensen, P. F. Staanum and M. Drewsen, *Angew. Chem., Int. Ed.*, 2012, **32**, 7960–7962.

27 C. W. Chou, C. Kurz, D. B. Hume, P. N. Plessow, D. R. Leibrandt and D. Leibfried, *Nature*, 2017, **545**, 203–207.

28 K. Mølhave and M. Drewsen, *Phys. Rev. A*, 2000, **62**, 011401.

29 N. Kimura, K. Okada, T. Takayanagi, M. Wada, S. Ohtani and H. A. Schuessler, *Phys. Rev. A*, 2011, **83**, 033422.

30 C. Becker, P. Casavecchia and P. Tiedemann, *J. Chem. Phys.*, 1980, **73**, 2833.

31 D. He, J. Yuan, H. Li and M. Chen, *J. Chem. Phys.*, 2016, **145**, 234312.

32 R. S. Tan, H. C. Zhai, W. Yan, F. Gao and S. Y. Lin, *J. Chem. Phys.*, 2017, **146**, 164305.

33 Z. Yang, H. Chen, Y. Mao and M. Chen, *Phys. Chem. Chem. Phys.*, 2022, **24**, 19209–19217.

34 H. J. Werner and P. J. Knowles, *J. Chem. Phys.*, 1988, **89**, 5803–5814.

35 P. J. Knowles and H.-J. Werner, *Chem. Phys. Lett.*, 1985, **115**, 259–267.

36 H. J. Werner, P. J. Knowles, G. Knizia, F. R. Manby and M. Schütz, *Wiley Interdiscip. Rev.: Comput. Mol. Sci.*, 2012, **2**, 242–253.

37 A. J. Dobbyn and P. J. Knowles, *Mol. Phys.*, 1997, **91**, 1107–1124.

38 D. M. Williams, A. Viel and W. Eisfeld, *J. Chem. Phys.*, 2019, **151**, 164118.

39 D. M. Williams and W. Eisfeld, *J. Phys. Chem. A*, 2020, **124**, 7608–7621.

40 C. Xie, C. L. Malbon, D. R. Yarkony and H. Guo, *J. Chem. Phys.*, 2017, **147**, 044109.

41 C. Xie, X. Zhu, D. R. Yarkony and H. Guo, *J. Chem. Phys.*, 2018, **149**, 144107.

42 Z. Sun, H. Guo and D. H. Zhang, *J. Chem. Phys.*, 2010, **132**, 084112.

43 Z. Sun, X. Lin, S. Y. Lee and D. H. Zhang, *J. Phys. Chem. A*, 2009, **113**, 4145–4154.